Chemical Science

ROYAL SOCIETY OF CHEMISTRY

EDGE ARTICLE

View Article Online
View Journal | View Issue

Cite this: *Chem. Sci.*, 2026, **17**, 5712

All publication charges for this article have been paid for by the Royal Society of Chemistry

Received 15th October 2025
Accepted 22nd January 2026

DOI: 10.1039/d5sc07961f

rsc.li/chemical-science

Toward functional and structurally complex Frank–Kasper phases *via* creating concavities on supramolecular micelles

Yong-Rui Wang,[a] Jui-Heng Weng,[a] Shing-Jong Huang,[a] Chun-Jen Su,[b] U-Ser Jeng,[b] Po-Ya Chang,[b] Wei-Tsung Chuang *[b] and Chien-Lung Wang *[a]

In supramolecular chemistry, higher structural complexity enables emergent functions in ordered soft matter. To construct structurally complex and functional Frank–Kasper (FK) phases, heterogeneity in supramolecular micelles is introduced by blending rigid aromatic dendrons (Ar_2) with flexible aliphatic dendrons (D_2). This approach creates micelles with surface concavities while preserving long-range periodicity of the FK σ lattice. The concave domains serve as enzyme-like pockets that accommodate guest molecules and facilitate photodimerization reactions. Structural analyses confirm that these features enhance complexity in hierarchical architecture and enable catalytic performance. This work presents a versatile strategy for designing FK phases that integrate molecular recognition, supramolecular precision, and catalytic function within an ordered framework.

Introduction

Nature creates self-assembly systems that are precise, complex and dynamic to enable physiological functions that are essential for life.[1] In comparison to their natural counterparts, artificial supramolecular systems still exhibit relatively limited structural complexity and functionality. To address this gap, researchers often tune two key parameters: multiplicity, which introduces chemical diversity in molecular composition and function, and interconnections, which define the bonding modes and dynamic interactions between components.[2,3] Modulating these parameters can influence how individual components integrate into higher-order architectures. As this hierarchical integration becomes more sophisticated, the overall organization of the system may change, giving rise to emergent collective properties.[2,3]

One strategy to enhance complexity is the incorporation of aperiodicity within periodic lattices. In block copolymers, factors such as conformational asymmetry,[4–7] volume asymmetry,[8–10] compositional asymmetry,[11–15] *etc.* have been applied to create symmetry breaking that leads to structural complexity in the spherical phases.[16] Blending, in particular, provides a straightforward means of controlling both formation and stability of Frank–Kasper (FK) phases, where uneven interfacial curvature promotes non-spherical and multi-sized micellar motifs.[11,12,17–23] However, blending-based polydispersity mainly alters micelle size and shape, and therefore offers only limited ways to introduce new structural features. Creating additional levels of complexity—such as spatially defined chemical environments, anisotropic interfaces, or directional binding sites—without disrupting the integration of the original FK lattice remains challenging. For example, although blending block copolymers can effectively shift the phase behavior of mixed systems, the resulting structures often retain a single pre-existing ordered phase, without generating finer structural features or new functional elements within that lattice.[12] This highlights the difficulty of enhancing structural complexity while maintaining long-range order.

Dendrons and dendrimers offer a distinctive pathway to such complexity and structural features.[24,25] Their generation-dependent shape evolution,[26–28] precise molecular design,[26,29–32] and versatile end-group modifications[27,30,33,34] enable quasi-equivalent packing that relieves frustration and supports tetrahedrally close-packed FK lattices.[35] Consequently, dendrons assemble into a remarkable diversity of structures—including cubic,[27,29,30,35,36] tetragonal,[28,31,35,37,38] quasicrystalline,[28,37–39] hollow,[33,34,37] and even chiral micelles[34,39,40]—surpassing what is typically achievable with block copolymers.[31,37] In contrast, natural blended systems routinely exploit heterogeneity to generate structural multiplicity and dynamic functionality. Biological membranes, for instance, form compositionally heterogeneous microdomains such as lipid rafts, stabilized by cholesterol–sphingolipid interactions that enhance membrane responsiveness.[41–44] Likewise, protein binding pockets provide concave hydrophobic cavities that couple structure to function, enabling selective guest recognition and catalysis by pre-organizing substrates and

[a]*Department of Chemistry, National Taiwan University, No. 1, Sec. 4, Roosevelt Rd, Taipei 10617, Taiwan. E-mail: kclwang@ntu.edu.tw*

[b]*National Synchrotron Radiation Research Center, 101 Hsin-Ann Road, Hsinchu 30092, Taiwan. E-mail: weitsung@nsrrc.org.tw*

stabilizing transition states.[45–48] These examples illustrate how blending-derived heterogeneity can simultaneously increase the complexity and functional adaptability of an assembly.

Motivated by these natural design principles—and by the ability of dendrons to introduce controlled heterogeneity—we sought to install designed concavities onto the surface of FK-phase supramolecular micelles. Our goal was to elevate the structural sophistication of the spherical assemblies while preserving the symmetry breaking and long-range integration of the FK lattice. As illustrated in Scheme 1, the diaryl amphiphiles ($\mathbf{Ar_2}$) are used as molecular rafts that create heterogeneity in supramolecular micelles formed by the amphiphilic di-dendron ($\mathbf{D_2}$). $\mathbf{D_2}$ molecule has been synthesized as the intermediate product of the Janus dendrimers for many research.[49–59] In our previous study, $\mathbf{D_2}$ has demonstrated the ability to form FK σ phase with symmetry breaking.[59] Since the $\mathbf{Ar_2}$ molecules are smaller and more rigid than $\mathbf{D_2}$, blending the $\mathbf{Ar_2}$ and $\mathbf{D_2}$ in the supramolecular micelles could create both heterogeneity and concavities in the supramolecular micelles of the FK phase. Catalytic functions mimic the natural hydrophobic pockets may also be added to the complex FK phase as the concavities on top of the $\mathbf{Ar_2}$ motifs could encapsulate guest molecules. Our characterization data indicated that on top of the symmetry breaking, the presence of the raft-inspired building blocks $\mathbf{Ar_2}$ in the supramolecular micelles of $\mathbf{D_2}$ created additional structural features and function to the FK σ phase. The overall integration of the synthetic self-assembly system is thus upgraded as the presence of the $\mathbf{Ar_2}$ advances both hierarchical complexity and functional adaptability of the spherical phase. This innovation aligns with Lehn's vision of progressive complexity,[3] bridging the gap between structural sophistication and dynamic functionality in artificial self-assembly systems.

Results and discussion

Create concavities onto the FK σ phase

Schemes S1–S3 illustrate the synthetic routes for $\mathbf{D_2}$ and $\mathbf{Ar_2}$. The synthesis routes of these di-dendron molecules are referring to the published literature of dendron self-assembly.[59] The molecular structures of these compounds were confirmed by ^{1}H NMR, ^{13}C NMR, and mass spectrometry, as presented in Fig. S2–S15. To incorporate the $\mathbf{Ar_2}$ into $\mathbf{D_2}$, both $\mathbf{Ar_2}$ and $\mathbf{D_2}$ were co-dissolved in CH_2Cl_2. After solvent removal, $\mathbf{Ar_2}/\mathbf{D_2}$ mixtures with varying molar fractions of $\mathbf{Ar_2}$ ($X_{\mathbf{Ar_2}} = 0.1$, 0.2, 0.3 and 0.4) were obtained. The ordered phases of the mixtures were then prepared by heating to 150 °C—above the isotropization temperatures (T_i) of both $\mathbf{D_2}$ and $\mathbf{Ar_2}$ but below their decomposition thresholds (Fig. S16)—to ensure homogeneous mixing in the molten state. The resulting melts were cooled and annealed at 40 °C for 12 hours to facilitate self-assembly.

To confirm the uniform incorporation of molecular rafts into the ordered phase of $\mathbf{D_2}$, optical microscopy (OM) was employed for direct observation. As shown in Fig. 1a, macroscopic spherulitic structures were evident in the drop-cast samples of the $\mathbf{Py_2}/\mathbf{D_2}$ mixtures. With increasing $\mathbf{Py_2}$ content, the spherulitic morphology became increasingly disrupted. At $X_{\mathbf{Py_2}} = 0.4$, the emergence of dark aggregated domains suggests phase segregation of excess $\mathbf{Py_2}$. This conclusion is further supported by wide-angle X-ray scattering (WAXS) data (Fig. 1b), where distinct crystalline diffraction peaks attributed to $\mathbf{Py_2}$ are observed in the $X_{\mathbf{Py_2}} = 0.4$ sample. In contrast, WAXS profiles of samples with $X_{\mathbf{Py_2}} = 0.1 - 0.3$ display no sharp crystalline peaks, but instead feature a broad amorphous halo. This indicates that the spherulitic structures observed *via* OM do not

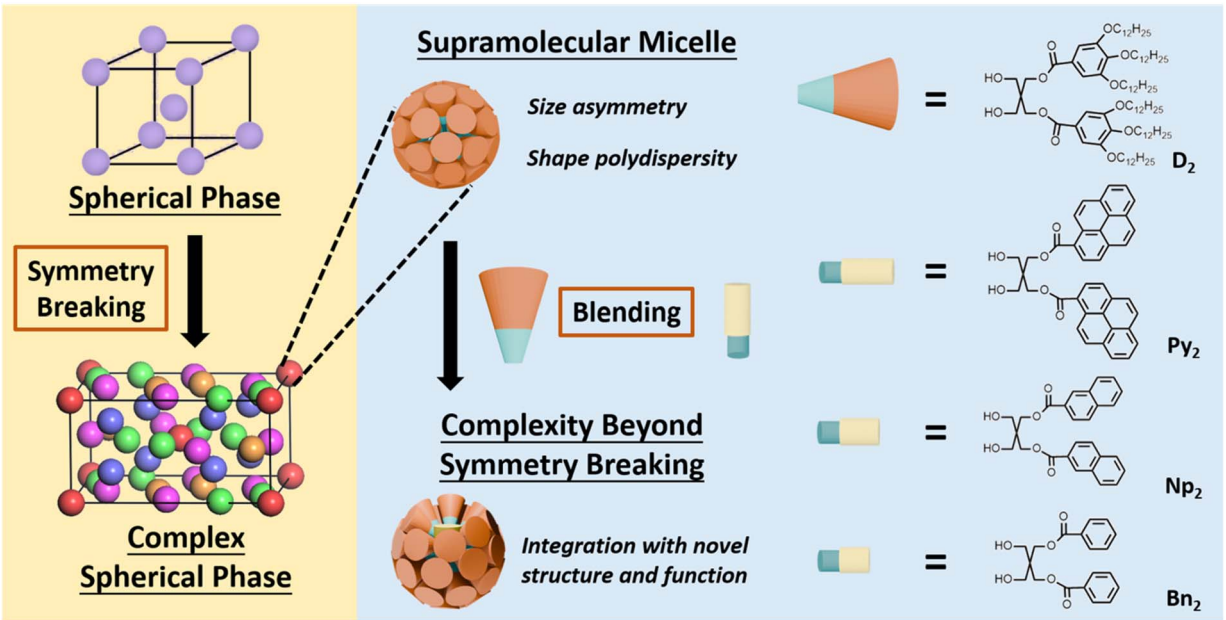

Scheme 1 (a) The element of complexity in the current FK phases – symmetry breaking. (b) Illustration of the strategy to further elevate the complexity in the FK phase – introducing heterogeneity and concavity by adding the molecular rafts – Ar_2 into the supramolecular micelles of D_2. The right panel shows the chemical structures of D_2 and the three Ar_2 molecules, Py_2, Np_2, and Bn_2.

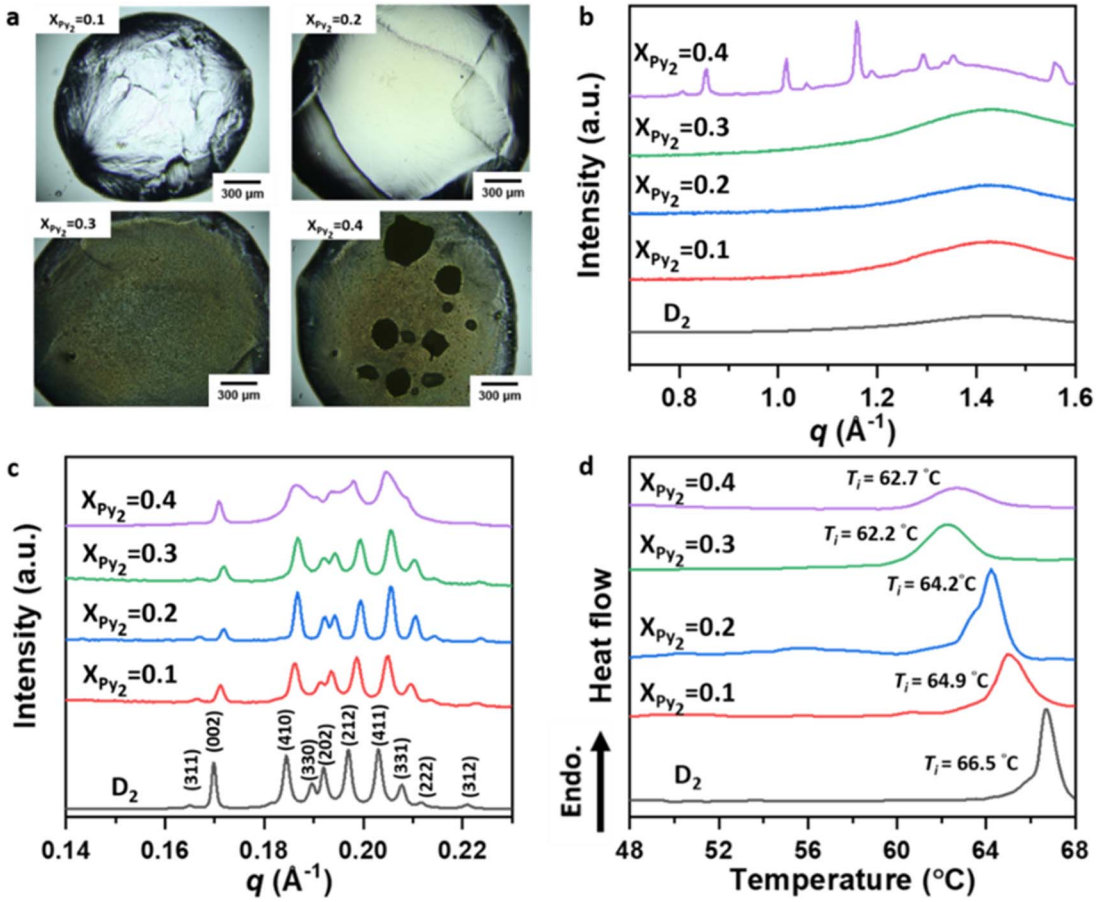

Fig. 1 (a) OM micrographs of drop-liquid samples. (b) WAXS and (c) SAXS patterns of the Py_2/D_2 mixtures. (d) DSC thermograms of the Py_2/D_2 mixtures. Note: (1) The lattice parameters of Py_2/D_2 mixtures and the diameter of these supramolecular micelles are shown in Table S2. (2) The DSC parameters of Py_2/D_2 mixtures are summarized in Table S3.

originate from angstrom-scale crystalline ordering. The scattering profiles of varies of **Ar_2** are shown in Fig. S17.

To probe the internal aggregate structures within these spherulites, small-angle X-ray scattering (SAXS) analysis was conducted (Fig. 1c). The SAXS profiles revealed that self-assemble micellization of the **Py_2**/**D_2** mixtures crystalizes into the FK σ phase. To further clarify how the SAXS data support the micellar assignment and FK σ phase formation, the primary and higher-order peaks were analyzed. The peak ratios (q/q_0) are consistent with the reflection pattern of the FK σ lattice,[60] and the comprehensive analysis of the σ-phase structure and its indexed diffraction peaks is provided in Table S1. The characteristic peaks q_{410}, q_{330}, and q_{002} were used to calculate the corresponding lattice parameters (a, b, c) by the standard geometric relations of tetragonal phase, shown in Table S2.[38] Based on these lattice parameters, the diameter of the supramolecular micelles within the FK σ lattice (D_{sphere}) was estimated, also performed in Table S2. These results confirm that the incorporation of **Py_2** does not inhibit the ability of **D_2** to act as a cone-shaped motif and self-assemble into the FK σ phase. However, the presence of **Py_2** shifts the diffraction peaks to higher q values and broadens them, indicating that the inclusion of rigid, small **Py_2** molecules introduces heterogeneity within the micelles and compresses the σ-phase lattice.

The formation of this FK σ phase from cone-shaped motifs represents a thermodynamically stable self-assembly, further validated by differential scanning calorimetry (DSC). As shown in Fig. 1d, the T_i of the mixtures systematically decreases with increasing **Py_2** content. This phase behavior is consistent with the principle of colligative properties, where the incorporation of solute molecules (**Py_2**) lowers the T_i of the host component (**D_2**).[61] This behavior also confirms that **Py_2** is well-dispersed within the **D_2**-rich ordered domains for compositions with $X_{Py_2} < 0.3$. At $X_{Py_2} = 0.4$, however, the T_i does not decrease further, indicating that the excess **Py_2** exceeds the micelle's incorporation capacity and instead undergoes phase separation to form **Py_2**-rich domains, as corroborated by both Fig. 1a and b. Additionally, the broadening of all (hkl) diffraction peaks in the SAXS profiles supports the DSC results, reinforcing the conclusion that **Py_2** molecules are randomly and uniformly distributed within the supramolecular micelles of **D_2**, resulting in both a reduction in T_i and broadened diffraction features.

The miscibility of other **Ar_2** variants—**Np_2** and **Bn_2**—with **D_2** was also assessed using the same protocol. The results, summarized in Fig. S18 and Tables S4–S9, confirm that both

Np_2 and **Bn_2** exhibit good miscibility with **D_2** up to $X_{Ar_2} \leq 0.3$. Moreover, increasing size mismatch between **Ar_2** and **D_2** leads to a greater suppression of T_i and more significant lattice contraction in the σ phase. This trend suggests that smaller molecular rafts introduce greater disruption to the micellar packing order, highlighting the influence of geometric compatibility on structural organization within FK σ phases.

The heterogeneity of the **Py_2/D_2** micelles and the dynamic behavior of **Py_2** within the supramolecular micelles were further investigated by solid-state ^{13}C–^{1}H heteronuclear correlation (HETCOR) nuclear magnetic resonance (NMR) spectroscopy. For pure **D_2** in the FK σ phase, cross-polarization (CP) is relatively inefficient due to the high segmental mobility; therefore, the HETCOR spectrum was acquired using a prolonged CP contact time (t_c) of 2 ms. In contrast, the HETCOR spectrum of **Py_2** was recorded with a short CP contact time of 200 μs to suppress undesired long-range polarization transfer.

As shown in Fig. 2a and b, the characteristic spectral features of **D_2** and **Py_2** are clearly distinguishable. For **D_2**, only cross-peaks originating from the dodecyl chains are observed, appearing in the ranges of $\delta_C = 10$–50 ppm and $\delta_H = 0$–3 ppm. In contrast, the expected resonances from the O–CH_2 units (δ_C

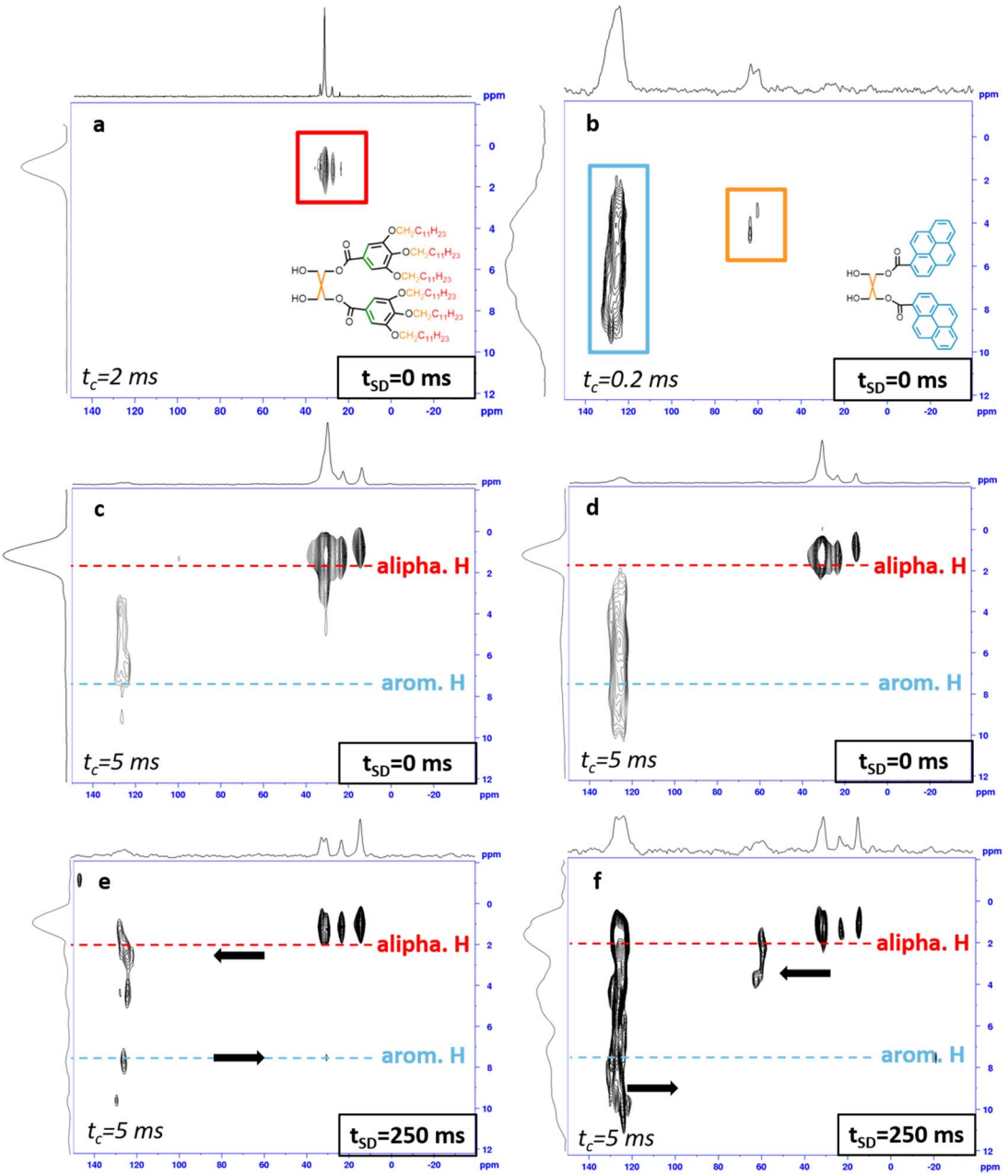

Fig. 2 (a) The ssNMR HETCOR spectra ($t_{SD} = 0$ ms) of pure D_2, (b) pure Py_2, (c) Py_2/D_2 mixture with $X_{Py_2} = 0.2$ and (d) Py_2/D_2 mixture with $X_{Py_2} = 0.3$. (e) The proton spin-diffusion- incorporated HETCOR spectra of the $X_{Py_2} = 0.2$ mixture at $t_{SD} = 250$ ms and (f) the $X_{Py_2} = 0.3$ mixture at $t_{SD} = 250$ ms.

≈ 65–75 ppm),[62] the pentaerythritol core (δ_C = 50–65 ppm and δ_H = 2–5 ppm), and the aromatic moieties (δ_C = 100–120 ppm and δ_H = 5–8 ppm) are absent. This behavior can be attributed to their significantly higher mobility, which leads to inefficient ^1H–^{13}C dipolar recoupling under the applied CP conditions, as discussed in detail in Fig. S19. For **Py_2**, in addition to the signals originating from the pentaerythritol core, an additional broad resonance at approximately $\delta_C \approx 120$ ppm was observed, which can be attributed to the **Py** segments. The aromatic ^1H signals of **Py_2** are widely distributed and predominantly broadened due to strong residual ^1H–^1H dipolar couplings that persist even under MAS conditions, as well as the heterogeneous local environments experienced by the **Py_2** segments within the micelles.[63–65] For the **Py_2**/**D_2** mixtures, the cross-peaks associated with **Py_2** are clearly observed in the HETCOR spectra for samples with X_{Py_2} = 0.2 and 0.3 in the HETCOR spectra, acquired with a prolonged contact time of 5 ms, as shown in Fig. 2c and d. In contrast, the **Py_2** signals in the X_{Py_2} = 0.1 mixture are too weak to be detected (Fig. S20) owing to the low **Py_2** concentration. To gain deeper insight into the location and orientation of the **Py** segments within the micelles, a ^1H spin-diffusion (PSD) block was incorporated into the HETCOR pulse sequence, rather than further extending the CP contact time, in order to probe long-range intermolecular spatial correlations. This strategy was adopted for three main reasons. First, magnetization decay in the present approach is governed by T_1 relaxation, whereas an extended CP contact time is limited by $T_1\rho$ relaxation, and T_1 is typically much longer than $T_1\rho$. Second, ^1H–^1H dipolar interactions play a crucial role in long-range intermolecular magnetization transfer; however, the spin-locking RF field ramped linearly from 40 to 50 kHz during CP may partially suppress these dipolar interactions and thus hinder spin diffusion. Third, excessively long CP contact times (>50 ms) may lead to power-handling issues in commercial MAS probeheads. As shown in Fig. 2e and f, at a spin-diffusion time (t_{SD}) of 250 ms, magnetization from the ^1H nuclei of the dodecyl chains is efficiently transferred to the **Py_2** segments. This effective magnetization transfers between the dodecyl chains and the **Py** segments indicates that the **Py** segments of the molecular rafts are primarily located within the hydrophobic shell of the supramolecular micelles, as schematically illustrated in Scheme 2a.

According to the previous work in our group,[59] in the σ phase of **D_2**, each supramolecular micelle is constructed with *ca.* 19 cone-like **D_2** molecules. Therefore, at X_{Py_2} = 0.2 and 0.3, each supramolecular micelle of **Py_2**/**D_2** mixtures has to accommodate *ca.* 4 and 6 **Py_2** molecules, respectively. Combining the ssNMR results in Fig. 2 and the SAXS, WAXS and OM data in Fig. 1, it was found that the presence of **Py_2** creates structural heterogeneity to the supramolecular micelles of **D_2**, but the loading capacity of the micelles is limited, as 6 **Py_2** molecules in each micelle is effective enough to create crowded environment that slows down the dynamics of the molecular rafts. The maximum loading capacity of each micelle in the σ phase is about 6 **Py_2** molecules, as the higher molar ratio of **Py_2** in the mixture led to the phase-separated **Py_2**-rich domains.

A comparable diffusion-based experiment was carried out for the **Np_2**/**D_2** system at a molar fraction of 20%, following the same experimental strategy as used for the **Py_2**/**D_2** mixtures. As shown in Fig. S21, distinct intermolecular magnetization transfer between the aliphatic region of **D_2** and the aromatic resonances of **Np_2** was observed, indicating efficient spin diffusion between these components. This result demonstrates that replacing **Py_2** with a different aromatic molecular raft (**Ar_2**) leads to a similar spatial proximity between the aromatic segments and the dodecyl-chain-rich hydrophobic domains of the **D_2** supramolecular micelles. The **Np_2**/**D_2** diffusion data therefore support the generality of aromatic raft incorporation within concaved σ-phase micelles, rather than a behavior specific to the **Py_2** system.

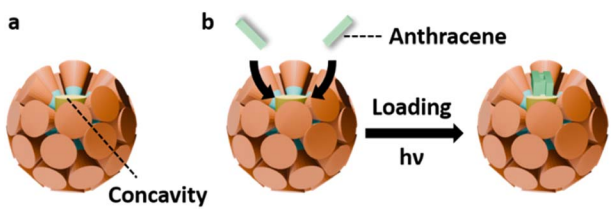

Scheme 2 (a) The surface cavity created by Ar_2 in the concaved supramolecular micelles of the σ(Ar_2). (b) The photodimerization catalytic process of anthracene within the concaved supramolecular micelle.

Guest encapsulation and catalytic properties of the σ(Ar_2)

As **D_2** and **Ar_2** are mismatch in size, incorporating molecular rafts **Ar_2** units into the supramolecular micelles of **D_2** create novel FK σ phases, denoted σ(**Ar_2**), which contain concave domains as illustrated in Scheme 2a. The indentations on the supramolecular micelles may provide confined environments for guest encapsulation and potential catalytic activation resembling hydrophobic enzyme pockets. To probe this, anthracene (**An**)—a planar polycyclic aromatic hydrocarbon structurally similar to the **Ar** segments—was selected as the guest molecule. Meanwhile, the [4 + 4] photodimerization of **An** molecules under UV light[66] was applied as the probe for both binding and reactivity within σ(**Ar_2**) with the molar ratio X_{Ar_2} = 0.2, as illustrated in Scheme 2b.

To differentiate the dispersion environments, the **An**-loaded assemblies are denoted as **An**@σ for the assemble using simply **D_2** as the host (conventional micelles), and **An**@σ(**Ar_2**) for those using **Ar_2**/**D_2** mixtures as the hosts (concaved micelles).

SAXS profiles in Fig. 3a shows that guest loading perturbs the lattice of conventional micelles, causing more significant lattice contraction and peak broadening of the σ phase of **D_2**, as shown in Table S11 and Table S12. The insignificant changes of the FK σ framework of σ(**Ar_2**) indicate that the pre-organized concavities localize guest molecules and reduce the extent of global lattice distortion. Due to the size differences, the incorporation of **Py_2**, **Np_2** and **Bn_2** results in concavities with difference depths in the micelles. Among the variants, σ(**Np_2**) provides the optimal balance of geometric complementarity and interaction strength, stably encapsulating 2 – 3 eq. of **An** without phase-

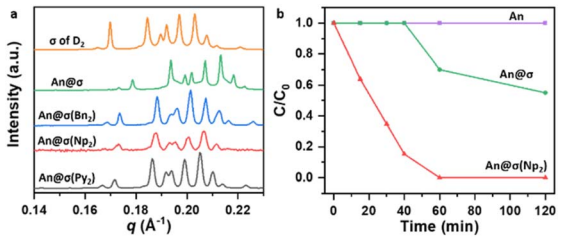

Fig. 3 (a) SAXS patterns of An@σ(Ar_2) and An@σ systems. (b) Normalized concentration of anthracene (C/C_0) plotted against irradiation time, monitored by ^{1}H NMR spectroscopy. Note: (1) the X_{Ar_2} is equal to 0.2 and the molar ratio of the encapsulated **An** and Ar_2 is 2 : 1 in the An@σ(Ar_2) samples. (2) The indexed diffraction peaks and the lattice parameters and diameter of the supramolecular micelle of **An**-loaded assemblies are shown in Tables S10 and S11. (3) The raw data of ^{1}H NMR spectroscopy for the photodimerization are shown in Fig. S24.

separation (Fig. S22 and S23). Collectively, these results establish that only concavities of suitable depth enable stable guest encapsulation, with σ(**Np$_2$**) standing out by accommodating two **An** per concavity—precisely the stoichiometry for photodimerization—highlighting the unique role of geometry-tuned concavities in stabilizing and pre-organizing guests.

Since σ(**Np$_2$**) exhibited the most favorable guest encapsulation, we next evaluated its impact on photoreactivity. As shown in Fig. 3b, crystalline **An** dimerized very slowly under UV irradiation ($\lambda = 365$ nm) due to the rigid packing of the lattice. In contrast, **An** dispersed in conventional micelles (**An**@σ) reached about 45% conversion within 2 h, consistent with the requirement for suitable intermolecular orientation;[67] the modestly improved conversion can be attributed to the greater molecular mobility in the fluidic micellar environment. Remarkably, in σ(**Np$_2$**) assemblies nearly complete photodimerization occurred within 1 h, demonstrating that the concavities not only stabilize guest encapsulation but also promote effective preorganization of the reactants. Collectively, these results show that concavity-engineered micelles enhance photoreactivity through the combined effects of confinement and spatial preorganization, thereby closely emulating the functional characteristics of enzymatic active sites.

Conclusions

To exceed complexity of the FK phase and equip functions to the bulk phase supramolecular micelles, in this study, aromatic (**Ar$_2$**) and aliphatic (**D$_2$**) dendrons are blended in controlled ratios to introduce heterogeneity and create surface concavities within the micellar domains of FK σ phase. These concavities increase architectural hierarchy through localized asymmetry while preserving the long-range periodicity of the FK σ lattice, as evidenced by SAXS and WAXS results. Solid-state NMR reveals that aromatic segments of the **Ar$_2$** reside in the hydrophobic micellar shell, confirming the formation of chemically distinct, heterogeneous domains. These features generate concavities that act as functional pockets for guest encapsulation without disrupting the FK σ lattice. SAXS and WAXS analyses confirm the incorporation of **An** into the ordered σ(**Np$_2$**) framework, revealing concavities with optimal depth and packing to encapsulate the guest molecules. Building on this structural evidence, time-dependent *ex situ* ^{1}H NMR demonstrates that such concavities substantially accelerate **An** photodimerization, as reflected in the C/C_0 profiles.

Together, these findings establish σ(**Np$_2$**) as the most effective architecture for promoting photoreactivity. More broadly, they highlight a generalizable strategy in which concavity confinement, molecular recognition, and dynamic guest exchange are embedded within a FK σ lattice, thereby functionally mimicking enzymatic active sites and advancing Lehn's vision of progressively complex soft materials.

Author contributions

Conceptualization, data curation, formal analysis: Y. R. W, J. H. W, W. T. C., and C. L. W. Funding acquisition: C. L. W. Investigation: Y. R. W, J. H. W, and S. J. H. Methodology: Y. R. W., S. J. H., and C. L. W. Project administration: Y. R. W., and C. L. W. Resources, software: S. J. H, C. J. S, U. S. J., P. Y. C., W. T. C., and C. L. W. Supervision, validation: W. T. C., and C. L. W. Visualization, writing – original draft: Y. R. W, and C. L. W. Writing – review & editing: Y. R. W, S. J. H., W. T. C and C. L. W.

Conflicts of interest

There are no conflicts to declare.

Data availability

All data supporting the findings of this study, including time-dependent ^{1}H NMR spectra, SAXS/WAXS scattering profiles, ssNMR spectra, TGA and DSC thermograms, are provided in the supplementary information (SI). Additional raw data generated and analyzed during the current study are available from the corresponding author upon reasonable request. Supplementary information: the synthetic procedures, ^{1}H and ^{13}C NMR and MASS spectrum and TGA and DSC thermograms of the **D$_2$** and **Ar$_2$**, Miller indices, lattice parameters, and S/WAXS patterns of FK σ phase of the **Ar$_2$**/**D$_2$** mixtures, instrumentation of the analytical experiments, ssNMR results and its pulse sequences, characterization and catalytic analysis of **An**, **An**@σ, and **An**@σ(**Ar$_2$**). See DOI: https://doi.org/10.1039/d5sc07961f.

Acknowledgements

We gratefully acknowledge the TPS 13A beamline at the National Synchrotron Radiation Research Center (NSRRC), Taiwan, for providing access to the S/WAXS measurements. Thermogravimetric analysis (TGA) was performed using the Thermal Analysis System at the Instrumentation Center, National Taiwan University (NTU). Mass spectrometry services were provided by the Consortia of Key Technologies, NTU. We also thank Dr Hsi-Ching Tseng at the NTU Instrumentation Center for the kind assistance with NMR measurements. This

work was supported by the National Science and Technology Council, Taiwan (NSTC 113-2123-M-002-008).

Notes and references

1 R. Montis, L. Fusaro, A. Falqui, M. B. Hursthouse, N. Tumanov, S. J. Coles, T. L. Threlfall, P. N. Horton, R. Sougrat and A. Lafontaine, *Nature*, 2021, **590**, 275–278.
2 J.-M. Lehn, *Science*, 2002, **295**, 2400–2403.
3 J. M. Lehn, *Angew. Chem., Int. Ed.*, 2013, **52**, 2836–2850.
4 Z. Gan, Z. Xu, K. Tian, D. Zhou, L. Li, Z. Ma, R. Tan, W. Li and X.-H. Dong, *Nat. Commun.*, 2024, **15**, 6581.
5 K. K. Lachmayr, C. M. Wentz and L. R. Sita, *Angew. Chem., Int. Ed.*, 2020, **59**, 1521–1526.
6 M. W. Bates, J. Lequieu, S. M. Barbon, R. M. Lewis III, K. T. Delaney, A. Anastasaki, C. J. Hawker, G. H. Fredrickson and C. M. Bates, *Proc. Natl. Acad. Sci. U. S. A.*, 2019, **116**, 13194–13199.
7 A. Reddy, M. S. Dimitriyev and G. M. Grason, *Nat. Commun.*, 2022, **13**, 2629.
8 A. Reddy, M. B. Buckley, A. Arora, F. S. Bates, K. D. Dorfman and G. M. Grason, *Proc. Natl. Acad. Sci. U. S. A.*, 2018, **115**, 10233–10238.
9 Y. Wang, J. Huang, X. Y. Yan, H. Lei, X. Y. Liu, Q. Y. Guo, Y. Liu, T. Liu, M. Huang and F. Bian, *Angew. Chem.*, 2022, **134**, e202200637.
10 A. Reddy and G. M. Grason, *Nat. Chem.*, 2019, **11**, 865–867.
11 M. Liu, Y. Qiang, W. Li, F. Qiu and A.-C. Shi, *ACS Macro Lett.*, 2016, **5**, 1167–1171.
12 A. P. Lindsay, R. M. Lewis III, B. Lee, A. J. Peterson, T. P. Lodge and F. S. Bates, *ACS Macro Lett.*, 2020, **9**, 197–203.
13 K. K. Lachmayr and L. R. Sita, *Angew. Chem., Int. Ed.*, 2020, **59**, 3563–3567.
14 H. Takagi and K. Yamamoto, *Macromolecules*, 2019, **52**, 2007–2014.
15 A. B. Chang and F. S. Bates, *ACS Nano*, 2020, **14**, 11463–11472.
16 S. Lee, C. Leighton and F. S. Bates, *Proc. Natl. Acad. Sci. U. S. A.*, 2014, **111**, 17723–17731.
17 Z. Xu and W. Li, *Chin. J. Chem.*, 2022, **40**, 1083–1090.
18 G. S. Doerk, A. Stein, S. Bae, M. M. Noack, M. Fukuto and K. G. Yager, *Sci. Adv.*, 2023, **9**, eadd3687.
19 J. Xie and A.-C. Shi, *Langmuir*, 2023, **39**, 11491–11509.
20 H. Lei, X.-Y. Liu, Y. Wang, X.-H. Li, X.-Y. Yan, T. Liu, J. Huang, W. Li, L. Wang, X. Kuang, X. Miao, F. Bian, M. Huang, Y. Liu and S. Z. Cheng, *J. Am. Chem. Soc.*, 2024, **146**, 33403–33412.
21 X.-Y. Liu, X.-Y. Yan, Y. Liu, H. Qu, Y. Wang, J. Wang, Q.-Y. Guo, H. Lei, X.-H. Li, F. Bian, X.-Y. Cao, R. Zhang, Y. Wang, M. Huang, Z. Lin, E. W. Meijer, T. Aida, X. Kong and S. Z. Cheng, *Nat. Mater.*, 2024, **23**, 570–576.
22 X.-Y. Yan, Q.-Y. Guo, X.-Y. Liu, Y. Wang, J. Wang, Z. Su, J. Huang, F. Bian, H. Lin, M. Huang, Z. Lin, T. Liu, Y. Liu and S. Z. Cheng, *J. Am. Chem. Soc.*, 2021, **143**, 21613–21621.
23 Y. Liu, T. Liu, X.-Y. Yan, Q.-Y. Guo, H. Lei, Z. Huang, R. Zhang, Y. Wang, J. Wang, F. Liu, F.-G. Bian, E. W. Meijer, T. Aida, M. Huang and S. Z. Cheng, *Proc. Natl. Acad. Sci. U. S. A.*, 2022, **119**, e2115304119.
24 B. M. Rosen, C. J. Wilson, D. A. Wilson, M. Peterca, M. R. Imam and V. Percec, *Chem. Rev.*, 2009, **109**, 6275–6540.
25 V. Percec, S. Wang, N. Huang, B. E. Partridge, X. Wang, D. Sahoo, D. J. Hoffman, J. Malineni, M. Peterca and R. L. Jezorek, *J. Am. Chem. Soc.*, 2021, **143**, 17724–17743.
26 V. Percec, W.-D. Cho, P. Mosier, G. Ungar and D. Yeardley, *J. Am. Chem. Soc.*, 1998, **120**, 11061–11070.
27 V. Percec, W.-D. Cho and G. Ungar, *J. Am. Chem. Soc.*, 2000, **122**, 10273–10281.
28 V. Percec, C. M. Mitchell, W.-D. Cho, S. Uchida, M. Glodde, G. Ungar, X. Zeng, Y. Liu, V. S. Balagurusamy and P. A. Heiney, *J. Am. Chem. Soc.*, 2004, **126**, 6078–6094.
29 V. Percec, C.-H. Ahn, G. Ungar, D. Yeardley, M. Möller and S. Sheiko, *Nature*, 1998, **391**, 161–164.
30 V. Percec, W.-D. Cho, G. Ungar and D. J. Yeardley, *J. Am. Chem. Soc.*, 2001, **123**, 1302–1315.
31 G. Ungar, Y. Liu, X. Zeng, V. Percec and W.-D. Cho, *Science*, 2003, **299**, 1208–1211.
32 S. Hudson, H.-T. Jung, V. Percec, W.-D. Cho, G. Johansson, G. Ungar and V. Balagurusamy, *Science*, 1997, **278**, 449–452.
33 V. Percec, B. C. Won, M. Peterca and P. A. Heiney, *J. Am. Chem. Soc.*, 2007, **129**, 11265–11278.
34 V. Percec, M. Peterca, A. E. Dulcey, M. R. Imam, S. D. Hudson, S. Nummelin, P. Adelman and P. A. Heiney, *J. Am. Chem. Soc.*, 2008, **130**, 13079–13094.
35 X. Zeng, G. Ungar, Y. Liu, V. Percec, A. E. Dulcey and J. K. Hobbs, *Nature*, 2004, **428**, 157–160.
36 V. Percec, W.-D. Cho, M. Möller, S. A. Prokhorova, G. Ungar and D. J. Yeardley, *J. Am. Chem. Soc.*, 2000, **122**, 4249–4250.
37 B. M. Rosen, D. A. Wilson, C. J. Wilson, M. Peterca, B. C. Won, C. Huang, L. R. Lipski, X. Zeng, G. Ungar and P. A. Heiney, *J. Am. Chem. Soc.*, 2009, **131**, 17500–17521.
38 M. N. Holerca, D. Sahoo, B. E. Partridge, M. Peterca, X. Zeng, G. Ungar and V. Percec, *J. Am. Chem. Soc.*, 2018, **140**, 16941–16947.
39 V. Percec, M. R. Imam, M. Peterca, D. A. Wilson, R. Graf, H. W. Spiess, V. S. Balagurusamy and P. A. Heiney, *J. Am. Chem. Soc.*, 2009, **131**, 7662–7677.
40 V. Percec, M. R. Imam, M. Peterca, D. A. Wilson and P. A. Heiney, *J. Am. Chem. Soc.*, 2009, **131**, 1294–1304.
41 D. Lingwood and K. Simons, *Science*, 2010, **327**, 46–50.
42 A. J. Sodt, M. L. Sandar, K. Gawrisch, R. W. Pastor and E. Lyman, *J. Am. Chem. Soc.*, 2014, **136**, 725–732.
43 K. Simons and D. Toomre, *Nat. Rev. Mol. Cell Biol.*, 2000, **1**, 31–39.
44 L. Rajendran and K. Simons, *J. Cell Sci.*, 2005, **118**, 1099–1102.
45 P. Setny and M. Geller, *J. Chem. Phys.*, 2006, 125.
46 A. K. Shrive, G. M. Gheetham, D. Holden, D. A. Myles, W. G. Turnell, J. E. Volanakis, M. B. Pepys, A. C. Bloomer and T. J. Greenhough, *Nat. Struct. Mol. Biol.*, 1996, **3**, 346–354.
47 J. W. Barnett, M. R. Sullivan, J. A. Long, D. Tang, T. Nguyen, D. Ben-Amotz, B. C. Gibb and H. S. Ashbaugh, *Nat. Chem.*, 2020, **12**, 589–594.

48 M. Yoshizawa, T. Kusukawa, M. Kawano, T. Ohhara, I. Tanaka, K. Kurihara, N. Niimura and M. Fujita, *J. Am. Chem. Soc.*, 2005, **127**, 2798–2799.
49 Q. Xiao, M. Delbianco, S. E. Sherman, A. M. Reveron Perez, P. Bharate, A. Pardo-Vargas, C. Rodriguez-Emmenegger, N. Y. Kostina, K. Rahimi and D. Söder, *Proc. Natl. Acad. Sci. U. S. A.*, 2020, **117**, 11931–11939.
50 V. Percec, P. Leowanawat, H.-J. Sun, O. Kulikov, C. D. Nusbaum, T. M. Tran, A. Bertin, D. A. Wilson, M. Peterca and S. Zhang, *J. Am. Chem. Soc.*, 2013, **135**, 9055–9077.
51 D. Zhang, E. N. Atochina-Vasserman, D. S. Maurya, N. Huang, Q. Xiao, N. Ona, M. Liu, H. Shahnawaz, H. Ni and K. Kim, *J. Am. Chem. Soc.*, 2021, **143**, 12315–12327.
52 C. Rodriguez-Emmenegger, Q. Xiao, N. Y. Kostina, S. E. Sherman, K. Rahimi, B. E. Partridge, S. Li, D. Sahoo, A. M. Reveron Perez and I. Buzzacchera, *Proc. Natl. Acad. Sci. U. S. A.*, 2019, **116**, 5376–5382.
53 N. Yu. Kostina, D. Söder, T. Haraszti, Q. Xiao, K. Rahimi, B. E. Partridge, M. L. Klein, V. Percec and C. Rodriguez-Emmenegger, *Angew. Chem., Int. Ed.*, 2021, **60**, 8352–8360.
54 S. Zhang, R. O. Moussodia, H. J. Sun, P. Leowanawat, A. Muncan, C. D. Nusbaum, K. M. Chelling, P. A. Heiney, M. L. Klein and S. André, *Angew. Chem.*, 2014, **126**, 11079–11083.
55 S. E. Sherman, Q. Xiao and V. Percec, *Chem. Rev.*, 2017, **117**, 6538–6631.
56 N. Huang, Q. Xiao, M. Peterca, X. Zeng and V. Percec, *Mol. Phys.*, 2021, **119**, e1902586.
57 V. Percec, D. A. Wilson, P. Leowanawat, C. J. Wilson, A. D. Hughes, M. S. Kaucher, D. A. Hammer, D. H. Levine, A. J. Kim and F. S. Bates, *Science*, 2010, **328**, 1009–1014.
58 L.-C. Lee and Y. Zhao, *J. Am. Chem. Soc.*, 2014, **136**, 5579–5582.
59 C.-L. Wang, W.-T. Chuang, M.-T. Lee, Y.-R. Wang, S.-Y. Chen, H.-J. Huang, S.-Y. Liu, J.-M. Lin, C.-Y. Chen and Y.-C. Lee, *ACS Appl. Mater. Interfaces*, 2025, **17**, 31403–31410.
60 T. Jun, H. Park, S. Jeon, S. Jo, H. Ahn, W.-D. Jang, B. Lee and D. Y. Ryu, *J. Am. Chem. Soc.*, 2021, **143**, 17548–17556.
61 H.-Y. Lin, B.-J. Zhong, H.-J. Liu, Y.-K. Wu, C.-H. Peng and C.-L. Wang, *Cryst. Growth Des.*, 2024, **24**, 2833–2840.
62 M. Seo, G. Seo and Y. K. Sang, *Angew. Chem., Int. Ed.*, 2006, **45**, 6306–6310.
63 C. S. Yannoni, *Acc. Chem. Res.*, 1982, **15**, 201–208.
64 L.-Q. Wang, J. Liu, G. J. Exarhos, K. Y. Flanigan and R. Bordia, *J. Phys. Chem. B*, 2000, **104**, 2810–2816.
65 F. G. Vogt, J. S. Clawson, M. Strohmeier, A. J. Edwards, T. N. Pham and S. A. Watson, *Cryst. Growth Des.*, 2009, **9**, 921–937.
66 H. Bouas-Laurent, A. Castellan, J.-P. Desvergne and R. Lapouyade, *Chem. Soc. Rev.*, 2000, **29**, 43–55.
67 S. L. Anderson, P. G. Boyd, A. Gładysiak, T. N. Nguyen, R. G. Palgrave, D. Kubicki, L. Emsley, D. Bradshaw, M. J. Rosseinsky and B. Smit, *Nat. Commun.*, 2019, **10**, 1612.